SITE PROPERTIES INFERRED FROM DELANEY PARK DOWNHOLE ARRAY IN ANCHORAGE, ALASKA

Erol Kalkan[1], Hasan S. Ulusoy[2], Weiping Wen[3], Jon. P. B Fletcher[1], Fei Wang[4] and Nori Nakata[5]

[1]*Earthquake Science Center, U. S. Geological Survey, CA, 94025, USA*

[2]*Consulting Engineer, Palo Alto, CA, USA*

[3] *Key Lab of Structures Dynamic Behavior and Control of the Ministry of Education, Harbin Institute of Technology, Harbin, 150090, China*

[4]*Earthquake Administration of Beijing Municipality, Beijing, China*

[5]*Department of Geophysics, Stanford University, CA, 94305, USA*

ABSTRACT

Waveforms recorded at various borehole depths were used to quantify site properties including predominant frequencies, shear-wave velocity profile, shear modulus, soil damping and site amplification at Delaney Park in downtown Anchorage, Alaska. The waveforms recorded by surface and six boreholes (up to 61 m depth) three-component accelerometers were compiled from ten earthquakes that occurred from 2006 to 2013 with moment magnitudes between 4.5 and 5.4 over a range of azimuths at epicentral distances of 11 to 162 km. The deconvolution of the waveforms at various borehole depths on horizontal sensors with respect to the corresponding waveform at the surface provides upward (incident) and downward (reflected) traveling waves within the soil layers. The simplicity and similarity of the deconvolved waveforms from different earthquakes suggest that a one-dimensional shear-beam model is accurate enough to quantify the soil properties. The shear-wave velocities determined from different earthquakes are consistent, and agree well with the logging data; the deconvolution interferometry predicts the shear-wave velocities within 15% of the in-situ measurements. The site amplifications based on surface-to-downhole traditional spectral ratio (SSR), response spectral ratio (RSR), cross-spectral ratio (cSSR), and horizontal-to-vertical spectral ratio (HVSR) of the surface recordings were also evaluated. Based on cSSR, the site amplification was computed as 3.5 at 1.5 Hz (0.67 s), close to the predominant period of the soil column. This amplification agrees well with the average amplification reported in and around Anchorage by previous studies.

Keywords: Site amplification, downhole array, wave propagation, interferometry, deconvolution, shear-wave velocity, spectral analysis, Bootlegger Cove formation.

INTRODUCTION

Anchorage, Alaska, lies within one of the most active tectonic environments, and thus has been subjected to frequent seismic activity. The city is built on the edge of a deep sedimentary basin at the foot of Chugach Mountain Range. The basin is over 1 km in thickness in the western part of Anchorage, and reaches 7 km depth at a point about 150 km southwest of the city (Hartman et al., 1974). Shear-wave velocities, measured at 36 sites (Nath et al., 1997) in the basin, indicate that most of the city is on sediments that fall in National Earthquake Hazard Reduction Program (NEHRP) site categories C ($360 < V_{S30} < 760$ m/s; V_{S30} = average shear-wave velocity of upper 30 m of crust) and D ($180 < V_{S30} < 360$ m/s) (Boore, 2004). The existence of low-velocity sediments overlying metamorphic bedrock can produce strong seismic waves (Borcherdt, 1970). The Great Alaskan earthquake (a.k.a. Prince William Sound earthquake) with moment magnitude (**M**) 9.2 in March 27, 1964, damaged the city, creating extensive liquefaction, landslides and subsidence as large as 3 m in the downtown area (Updike and Carpenter, 1986; Lade et al., 1988), and moved much of coastal Alaska seaward at least 80 m due to ground failures (Brocher et al., 2014).

In 2003, the U.S. Geological Survey's (USGS) Advanced National Seismic System established a seven-level downhole array of three-component accelerometers at Delaney Park in downtown Anchorage in order to measure sediments response to earthquake shaking, and to provide input wave-field data for soil-structure interaction studies of a nearby twenty-story steel moment frame building (Atwood Building), also instrumented. Figure 1 shows the photo and map view of this downhole array (henceforth denoted as DPK) and Atwood Building in the background. The deepest downhole sensors are located at 61 m depth within the soil layer corresponding to the engineering bedrock.

Since 2003, more than a dozen earthquakes with **M**4.5 and above have been recorded at the DPK. These recordings provide an excellent opportunity to extract the site properties, and compare them with those from the earlier studies. The waveforms used in this study are rich enough in low-frequency content that the site amplifications can be computed at low frequencies. First, we applied deconvolution interferometry to the waveforms from ten earthquakes in order to compute shear-wave velocity profile, shear modulus and soil damping. The deconvolution interferometry provides a simple model of wave propagation by considering correlation of motions at different observation points (e.g., Aki, 1957; Claerbout, 1968; Trampert et al. 1993; Lobkis and Weaver, 2001; Roux and Fink, 2003; Schuster et al., 2004; Bakulin and Calvert, 2006; Snieder et al., 2006). It also yields more repeatable and higher resolution wave-fields than does cross-correlation interferometry (Nakata and Snieder, 2012; Wen and Kalkan, 2016). Our approach is similar but we identified incident and reflected deconvolved waves and used time reversal to determine the site properties. Although deconvolution and cross-correlation interferometry are interrelated, we preferred the deconvolution interferometry for this study because the effects of the external source have been removed in the latter approach (Snieder and Safak, 2006; Rahmani and Todorovska, 2013). Second, we estimated predominant frequencies of the DPK array by utilizing a frequency response function (FRF), and also by using the average shear-wave velocity of the soil column. Third, the site amplification based on the surface-to-downhole traditional spectral ratio (SSR), response spectral ratio (RSR), cross-spectral ratio (cSSR), and horizontal-to-vertical spectral-ratio (HVRS) with surface recordings was evaluated and compared.

The complete list of abbreviations and symbols used throughout this article is given in Table 1.

TECTONIC SETTING

The Anchorage area is located in the upper Cook Inlet region. Cook Inlet is situated in a tectonic forearc basin that is bounded to the west by the Bruin Bay-Castle Mountain fault system and to the east by the Border Ranges fault system including the Knik fault along the west front of the Chugach Mountains as depicted in Figure 2 (Lade et al., 1988). Most of the regional seismicity can be attributed to under-thrusting along the Benioff zone (within ~150 km of Anchorage) of the plate boundary megathrust (Li et al., 2013). Large historical earthquakes have ruptured much of the length of this megathrust (Wong et al., 2010). The Benioff zone (its contour is shown by thick dashed line) dips to the northwest beneath the Cook Inlet region (Fogelman et al., 1978).

Smart et al. (1996) suggests that the Paleogene strike slip along the Border Ranges fault was transferred to dextral slip on the Castle Mountain fault through a complex fault array in the Matanuska Valley and strike-slip duplex systems in the northern Chugach Mountains. There is some evidence suggesting that both the Castle Mountain (Bruhn, 1979; Lahr et al., 1986) and Border Ranges fault systems (Updike and Ulery, 1986) may be active, and capable of propagating moderate size earthquakes. The Castle Mountain fault approaches to within about 40 km of the city. Each year earthquakes with moment magnitudes above 4.5 are felt in Anchorage as a result of this tectonic setting.

THE SITE, INSTRUMENTATION AND EARTHQUAKE DATA

DPK array is located at north-west downtown Anchorage as shown in map view in Figure 1. The geological section at the site consists of glacial outwash, overlying Bootlegger Cove formation (BCF) and glacial till deposited in a late Pleistocene glaciomarine-glaciodeltaic environment (14,000–18,000 years ago) (Ulery et al., 1983). The glacial outwash contains gravel, sand and silt, commonly stratified, deposited by glacial melt water. This surficial mud layer of soft estuarine silts overlays an approximately 35 m thick glacio-estuarine deposit of stiff to hard clays with interbedded lenses of silt and sand. This glacio-estuarine material is known locally as the BCF. Underlying the BCF is a glaciofluvial deposit from the early Naptowne glaciation (Updike and Carpenter, 1986) consisting mainly of dense to very dense sands and gravels with interbedded layers of hard clay (Finno and Zapata-Medina, 2014). The BCF (from 20-50 m depth) has major facies with highly variable physical properties (Updike and Ulery, 1986). Cone penetration test blow counts are down in the single digits at depths of over 30 m in BCF, and shear-wave velocity diminishes with depth through this formation (Steidl, 2006). The glacial till is composed of unsorted, nonstratified glacial drift consisting of clay, silt, sand and boulders transported and deposited by glacial ice. The relatively thin (<12.5 m) glacial outwash at the surface is locally underlain by sensitive facies of the BCF that could cause catastrophic failures during earthquakes, as occurred during the 1964 great Alaska earthquake. The DPK array has been deployed to sample the ground motions within this formation, as well as above and below it (Figure 3). The deepest borehole sensor is located in a glacial till formation with $V_S >$ 900 m/s, corresponding to engineering bedrock. Due to lack of in-situ measurements at the DPK site, the shear-wave velocity (V_S) of soil column have been estimated by Nath et al. (1997) and Yang et al. (2008) in Figure 4 from inversion of data at a nearby site, about 200 m away (U. Dutta, oral commun., 2014). The V_S increases initially within the glacial outwash at shallower depths, and then decreases within the deeper BCF.

The DPK array consists of one surface and six borehole tri-axial accelerometers located at

4.6, 10.7, 18.3, 30.5, 45.4 and 61 m depth, and oriented to cardinal directions as marked in Figure 3. These borehole depths do not correspond to the depth of the boundary of soil layers. The accelerometers in boreholes (Episensors) are connected to four six-channels 24-bit data loggers (Quanterra-330). More than a dozen earthquakes with **M**4.5 and above have been recorded since the deployment of the DPK array. Ten earthquakes with **M** between 4.5 and 5.4 were identified for this study based on their proximity to the site and recordings' intensity. The distant earthquakes were discarded due to low signal-to-noise ratio of the waveforms. The events selected are listed in Table 2 along with distance and epicenter. The event epicenters are depicted on a regional map in Figure 5; also shown in this figure are known faults around the city. Most of the events selected are 35–83 km deep, and 80% of records are considered as far-field since they were recorded at epicentral distances larger than 20 km. All earthquake data have a sampling rate of 200 samples-per-second with a minimum duration of 222 s, covering potential surface waves. The 2012 **M**4.6 earthquake is the closest event with a peak ground acceleration (PGA) of 1.8% g, recorded at epicentral distance of 10.8 km. The largest PGA of 3.1% g (see Figure 6) was recorded during the 2010 **M**4.9 event at epicentral distance of 20.7 km. Figure 6 shows the motions from glacial till amplify as they propagate within the BCF, and de-amplify within the transition region to glacial outwash due to impedance contrast.

DECONVOLUTION INTERFEROMETRY

A one-dimensional shear-beam model provides useful information about soil response to ground shaking (Iwan, 1997). For soil column with uniform mass and stiffness, the shear-wave propagation can be expressed in the time domain as:

$$u(t,z) = A(t,z) \cdot s\left(t - \frac{z}{c}\right) + A(t,2H - z) \cdot s\left(t - \frac{2H - z}{c}\right) +$$

$$r \cdot A(t,2H + z) \cdot s\left(t - \frac{2H+z}{c}\right) + r \cdot A(t,4H - z) \cdot s\left(t - \frac{4H-z}{c}\right) + \cdots \quad (1)$$

where $u(t,z)$ is the soil response at height z ($z = 0$ at the bottom of the borehole) at time t, $s(t)$ is the excitation source at the fixed-base, H is the total height, c is the traveling shear-wave speed, and r is the reflection coefficient at z = 0. r was assumed to be zero for the borehole case. The attenuation occurs during wave propagation in soil column when a wave travel over a distance L, which is described by attenuation operator $A(L,t)$. For a constant Q-model, this attenuation operator in frequency domain is given by Aki and Richards (2002):

$$A(w,L) = \exp\left(-\xi \cdot |w| \cdot L/c\right) \quad (2)$$

where w is the cyclic frequency defined as $2\pi/t$, ξ is the viscous damping ratio [ξ =$1/(2Q)$].

Equation (1) shows that the soil response is the summation of an infinite number of the upward and downward traveling waves. The first term is the upward traveling wave, and the second term represents the reflection of the first wave at the free end, and travels downward. This wave reflects off the fixed-base and travels upward, which is the third term. The last term is the reflection of the third wave at the free end, which travels downward. For the attenuation model in Equation (2), the soil response in the frequency domain is expressed as:

$$U(w,z) = \sum_{n=0}^{\infty} S(w)\, R^n \{\exp(i \cdot |k| \cdot (2n \cdot H + z)) \cdot \exp(-\xi \cdot |k| \cdot (2n \cdot H + z)) +$$

$$\exp\big(i \cdot |k| \cdot (2(n+1)H - z)\big) \cdot \exp\big(-\xi \cdot |k| \cdot (2(n+1)H - z)\big)\} \quad (3)$$

where $k = w/c$ is the wave number, i is the imaginary unit. The deconvolution of the response at height z by the response at the free end (surface for soil) is defined in frequency domain by

$$D(w, z) = U(w, z)/U(w, H) \quad (4)$$

By plugging equation (3) into equation (4), and making appropriate cancellations, $D(w, z)$ can be obtained as

$$D(w, z) = \frac{1}{2}\{\exp(i \cdot |k| \cdot (-H + z))exp(-\xi \cdot |k| \cdot (-H + z)) + \exp\big(i \cdot |k| \cdot (H - z)\big)\exp\big(-\xi \cdot |k| \cdot (H - z)\big)\} \quad (5)$$

Equation (5) shows that the soil response at height z deconvolved by the response at the surface is the summation of the two attenuated waves traveling upward and downward. Waveform deconvolution decouples the soil response from the excitation because this deconvolution is independent of the excitation source and the reflection coefficient (Snieder and Safak, 2006; Nakata et al., 2013). Hence, the soil properties can be estimated from the deconvolved waveforms.

RESULTS

We applied deconvolution interferometry to the data from ten earthquakes listed in Table 2. The soil responses $U(w, z)$ from six boreholes were deconvolved by the soil response measured at the surface $U(w,H)$. The deconvolution was based on the single component (east-west) of the horizontal motions because both horizontal components of records produced similar results. Figure 7 shows the waveforms in Figure 6 after deconvolution with the waves at the surface. Full lengths of the waveforms, low-cut filtered by a 4th order acausal Butterworth filter with corner frequency of 0.1 Hz, are used.

The deconvolved wave at the surface is a bandpass-filtered Dirac delta function (virtual source), because any waveform deconvolved with itself, with white noise added, yields a Dirac delta function (pulse) at t = 0 (see Equation (4) with z = H). The deconvolved waveforms at borehole-2 through borehole-6 demonstrate a wave state of the borehole array. This wave state is the response of different soil layers to the delta function at the surface. For early times, the pulse travels downward in the soil column with a velocity equal to shear-wave velocity of soil layers, and response is superposition of upward and downward traveling waves. At t = 0, the wave field is non-zero only at the surface. For later times, however, the waveforms are governed by site resonance that decays exponentially with time due to attenuation (intrinsic damping).

The deconvolved waves shown in Figure 7 contain energy in the acausal part (no phase shift). For negative time, upward going and downward going waves are present that reflect at the surface at t = 0. If the waveforms are deconvolved with the waveform at borehole-6, they will not display acausal arrivals; because there is no physical source at the surface, while the borehole-6 is being shaken by the earthquake. The shaking at the borehole-6 would act as an external source. The causality properties of the deconvolved waveforms are therefore related to the existence (or non-existence) of a physical source of the recorded waves (Snieder et al., 2006). The deconvolved waves in Figure 7 do not show notable intrinsic damping, but some pulse broadening is apparent. This is consistent with the soil-damping ratio computed (will be described later in "Soil-damping Ratio").

Shear-wave Velocity

The shear-wave velocity of the upward and downward traveling waves ($V_{S,n}$) for the n^{th} layer between two boreholes is derived based on the time lag τ between deconvolved waveforms and the distance following the ray theory, which ignores wave scattering, $V_{S,n} = h/\tau$, where h is the distance. The wave travel time (τ) associated with the first borehole at 4.6 m is discarded because of the overlapping upward and downward waves at this level. In Figure 8a and Figure 8b, the arrival time and travel distance of the upward and downward traveling waves are identified to compute the shear-wave velocity profiles based on the 2010 **M**4.9 earthquake waveforms shown in Figure 6. The negative values are due to the upward traveling waves, and the positive values are associated with the downward traveling waves. A straight line is fitted to all data points in Figure 8b by least squares with the Levenberg-Marquardt method (Levenberg, 1944; Marquardt, 1963) to determine a single average shear-wave velocity for the upper 61 m of the soil. Figure 8c depicts the shear-wave velocity of layers for the upward and downward traveling waves, and compares them with the logged data shown by horizontal bars; the deconvolution results in shear-wave velocities within 15% of the logged data. Note that the term "layer" used here does not necessarily refer to soil layers with distinct physical parameters but the soil medium between tips of two boreholes where the accelerometers are located, which are shown by dash lines in Figure 8c.

The same process is repeated for the remaining recordings from nine earthquakes, and Table 3 summarizes the shear-wave velocity of the soil layers for each event; also given at the last row of this table are the average shear-wave velocities considering all events. The difference of velocity for upward and downward traveling waves is due to reflection between soil layers, which creates epistemic noise. The shear-wave velocities of the five layers estimated from different earthquakes are very close to each other. Among all layers, the maximum discrepancy between different events is 17%. The last column of Table 3 lists the average shear-wave velocity for the upper 61 m of the soil column for each event computed according to the least square fit shown in Figure 8b. The average shear-wave velocities from the ten earthquakes are practically the same with a maximum discrepancy of 1.7%, indicating that site response remained linear-elastic between different events.

Soil Predominant Frequencies

For a homogenous isotropic soil medium with one-dimensional wave propagation model, the predominant frequency (f) of the soil column can be derived from the shear-wave velocity, $f = V_s/4H$ where H is the total height of the soil column. The predominant frequency derived by this simple equation for each earthquake is presented in Table 4. The average value of f is 1.2 Hz when all events are considered. For comparison, the predominant frequency of the soil is also computed from the FRF, defined as the surface response compared to the input of the deepest borehole following the initial work done by Borcherdt (1970) and then Joyner el al. (1976) for the San Francisco Bay. The FRF is computed as

$$H(f) = P_{xx}(f)/P_{xy}(f) \tag{6}$$

where P_{xx} is the power spectral density of the soil response measured at the surface, and P_{xy} is the cross power spectral density of the soil response measured at the surface and at the borehole-6. Note that Equation (6) is inverted compared to most uses of this method. Figure 10 plots the computed FRFs from ten events. The peaks around 5 to 6 Hz appear only for two events; we attributed these spurious peaks to limitation of the FRF method, and rejected them. The first three frequencies in the FRFs are listed in Table 4. The relative difference between the largest and lowest predominant frequencies is 12%. The relative differences between the largest and lowest second and the third frequencies are 5.6% and 3.2%, respectively. Average value of site fundamental frequency (first mode) from ten earthquakes is 1.44 Hz. For all earthquakes, the predominant frequency derived from the average shear-wave velocity of the soil column is 17% smaller than that computed from the FRF. This difference is expected because the frequency derived from the average shear-wave velocity is based on the assumption that the soil column has a uniform mass and stiffness. This assumption often yields smaller frequencies. The average ratios of the second and third frequencies to the predominant frequency are 2.8 and 4.8, respectively while the corresponding analytical ratios are 3 and 5 for uniform soil column.

Site Amplification

Site amplification refers to the increase in amplitude of seismic waves as they propagate through soft soil layers; this increase is the result of impedance contrast (impedance = density of soil x V_S) between different layers (Safak, 2001). A number of empirical site amplification studies have been published for the Anchorage area (e.g., Nath et al., 2002; Martirosyan et al., 2002; Dutta et al., 2003). The last two studies computed site response at the basin stations relative to a reference site in the nearby Chugach Mountains. All of the studies focused on site response within the 0.5 to 11 Hz range, and all of the studies found significant frequency-dependent site amplifications on the sediments beneath the city. The largest site amplifications on average were reported on the lower-velocity NEHRP class D sites, with average amplifications around 3 at low frequencies (0.5–2.5 Hz) and around 1.5 at higher frequencies (3.0–7.0 Hz).

Safak (2001) provides a review of various methods to estimate site amplifications. In this study, the site amplification is calculated with the following four different methods: (i) surface-to-borehole standard spectral ratio (SSR); (ii) surface-to-borehole cross-spectral ratio (cSSR); (iii) horizontal-to-vertical spectral ratio (HVSR); and (iv) surface-to-borehole response spectral ratio (RSR).

The SSR is the ratio of the Fourier spectra of the site recording to those of the reference-site recording. The deepest borehole in this study is selected as a reference because it is embedded to the engineering bedrock (glacial till). The borehole recording is influenced by the downward waves reflected by the soil layers above, and the destructive interference among these waves may cause unexpected peaks in the spectral ratios (Shearer and Orcutt, 1987; Steidl et al., 1996). When shallow borehole data are used as reference for estimating amplification at the surface, the potential maximum in the borehole spectrum would produce peaks in the spectral ratios that could be miscalculated as site-response peaks. Steidl et al. (1996) suggests that coherence estimate $C_{xy}(f)$ between the surface and borehole-recorded signals can be used to identify the destructive interference effects that manifest as artificial peaks in the surface-to-borehole transfer function. These artificial peaks correspond to the sinks in the coherence estimate.

In order to eliminate the effects of the destructive interference on site amplification, we computed the cSSR, which is the product of the spectral ratio and the coherence function (Safak, 1997), to estimate the site amplification (Assimaki et al., 2008). The coherence $C_{xy}(f)$ of the surface recording and borehole recording is computed as:

$$C_{xy}(f) = \frac{|P_{xy}(f)|^2}{P_{xx}(f)P_{yy}(f)} \quad . \tag{7}$$

$C_{xy}(f)$ ranges between zero and one, and it is used to assess the effects of noise in the waveform. Frequency ranges in the transfer function that are dominated by noise (typically high frequencies) demonstrate low coherence. At frequencies where sinks are observed in the coherence estimate, the resulting cross-spectral estimate of the transfer function is expected to deviate from the traditional spectral ratio, indicating the occurrence of destructive interference phenomena. Such phenomena (incoherence) can be due to noise or to natural physical processes such as wave passage, scattering and extended source effects (Zerva, 2009).

The HVSR is defined as the Fourier spectral ratio between the horizontal and vertical recordings (Nakamura, 1989). It is widely used to estimate the fundamental resonance mode at a site. The Fourier spectra of the horizontal recording are estimated by the root mean square of the Fourier spectra of two horizontal components (Martirosyan et al., 2002). HVSR of earthquake motions have also been used to identify the velocity profiles (Arai and Tokimatsu, 2004). A thorough review of the HVSR implementation can be found in Kudo et al. (2004). Studies showed that estimates of the frequency of the predominant peak from HVSR are similar to that obtained with traditional spectral ratios; however, the absolute level of site amplification does not correlate with the amplification obtained from more conventional methods (Lachet and Bard, 1994; Field and Jacob, 1995; Field, 1996; Lachet et al., 1996). Thus, HVSR is generally used to analyze the fundamental resonance peaks but not to determine precisely the amplification levels (Bonilla et al., 1997; Riepl et al., 1998; Parolai and Richwalski, 2004).

Finally, the RSR, defined as the ratio of 5% damped pseudo-spectral acceleration response spectrum on surface to those on the deepest borehole, was used (Kitagawa et al., 1992). Pseudo-spectral acceleration response spectra and their ratios are much smoother functions of frequency than the standard spectral ratios because the damped single-degree-of-freedom system acts as a narrow-band filter.

The ratio of the Fourier amplitude spectrum (FAS) of two noisy records is very sensitive to noise, and would have unrealistically high amplitudes if no smoothing were performed on the FAS prior to taking the ratio. Thus, we applied a moving average filter with a length of 2 s (0.5 Hz) for smoothing in computing the RSR, cSSR and HVSR.

For each of these four methods, site amplifications at different frequencies were computed and averaged across the ensemble of recordings considering all events. Figure 11 plots the mean estimates. Note that the DPK array site has a shallow soft layer in the near surface with relatively constant shear-wave velocity (295 m/s; NEHRP site category D) due to presence of BCF overlying a relatively homogeneous stiff formation with strong impedance contrast at 50 m depth (NEHRP site category B). In Figure 11, the values on the horizontal axis are the reciprocals of the periods for the RSR. For each method, three obvious peaks can be seen at three frequency ranges (1.1-1.5 Hz), (4.0-4.4 Hz) and (6.8-7.2 Hz), respectively. These peaks correspond to the predominant frequencies for the first three modes as shown in Figure 10. The SSR method produced the greater site amplification estimates than the cSSR and RSR methods with the exception of HVSR method at low frequencies. Although the frequencies of the predominant peaks from HVSR are similar, the absolute level of site amplification does not correlate well with the amplification estimated from other methods. The SSR method predicts the maximum site amplification as 5.3. This method is the least reliable because it is very sensitive to the noise level in the waveforms, thus it is not appropriate for downhole recordings.

The maximum site amplification of 4.2 is predicted by the RSR method; this method is applicable at low frequencies (e.g., less than 4 Hz), but not for high frequencies. The cSSR method resulted in maximum site amplification as large as 3.5 at low frequencies close to the first-mode frequency shown in Figure 10.

The average coherence estimates of the surface and the deepest borehole recordings are also presented in Figure 11. Based on the equivalent homogeneous medium approach (Steidl et al., 1996), the first mode frequency at which destructive interference is expected to occur is estimated as 1.2 Hz, which is also indicated in Figure 11 with the solid line arrow. Clearly, the destructive interference phenomena is not strictly materialized, which may due to the variation of the shear-wave velocity among different soil layers as can be seen in Figure 8c. However, the dashed line with arrows in Figure 11 indicate that peak site amplification predicted by SSR method generally corresponds to the sinks of coherence estimates. This phenomenon means that the cSSR method can predict site amplification at low frequencies more reliably by removing the potential destructive interference.

Soil-damping Ratio

During wave propagation, the energy loss induced by soil damping can be represented by the following attenuation equation (Aki and Richards, 2002):

$$A_s(f) = e^{-\pi \cdot f \cdot \tau / Q} \tag{8}$$

where $A_s(f)$ is the reduction in the amplitude of a sinusoidal wave of frequency f when it travels a distance of travel time τ. The damping ratio ξ is defined by the quality factor Q ($\xi = 1/2Q$).

In order to evaluate the dynamic damping in structures, previous studies (Snieder and Safak, 2006; Prieto et al., 2010; Newton and Snieder, 2012; Nakata et al., 2013) used the equation (8) in conjunction with deconvolved waves. We adapted the same approach for evaluating the soil dynamic damping. First, the recordings at different soil layers were deconvolved with the recordings at the deepest borehole, and then, the deconvolved waves were bandpass filtered by a 4th order Butterworth filter with cutoff frequencies of 0.5 and 2 Hz. These corner frequencies were selected to extract the fundamental mode, and filtered out high and low frequencies. The natural logarithm of the envelope of the bandpass-filtered waveforms corresponding to the **M**4.9 event is shown in Figure 11 by dashed lines. In order to separate the curves at different borehole depths, the natural logarithm of the envelope is added with the number of 50 minus the depth of the borehole (the depth is 0 at the surface). According to the equation (8), the slope of the curves in Figure 11 depends on the attenuation of the waves, thus the offset has no influence on the results. The slopes of the curves, which are similar at different layers, were computed by least-square fit between 0.5 s and 5.0 s (shown by solid lines). The slope of the solid line is equal to $-\pi f/Q$. The mean slope at different layers (which is quite consistent at different depths), and the first mode frequencies in Table 4 were used to compute the Q and ξ. Table 5 summarizes the resultant Q and ξ for all events. The results are stable between different events with a coefficient of variance of 0.16 for Q. The average soil dynamic damping for the DPK array was found to be 4.5%.

Shear Modulus

In homogeneous and isotropic media, the velocity of a shear wave is controlled by the shear modulus G_n, which defines the magnitude of the shear stress that soil can sustain—an important parameter for geotechnical engineering. The shear modulus G_n for the n^{th} soil layer is

$$G_n = \rho_n \cdot V_{S,n}^2 \tag{9}$$

where $\rho_n$is the density of the n^{th} layer. A wet density of 1.96 g/cm^3 was assigned to the BCF (from 20-50 m depth) based on measurements of ten soil samples (Lade et al., 1988). The site at which the undisturbed samples of the BCF were collected was found to be geologically typical of the 60 city blocks that form the metropolitan "core area" of Anchorage including the DPK array. Using equation (9) and shear-wave velocity values in Table 3, the shear modulus of the BCF at the DPK array was found to be between 125 and 170.9 MPa.

CONCLUSIONS

In this study, we investigated the linear-elastic properties of the sediment layers in particular the Bootlegger Cove formation (BCF) at Delaney Park (DPK) downhole array in downtown

Anchorage Alaska. BCF is a soft formation thought to be responsible for much of the liquefaction damage during the 1964 **M**9.2 great Alaska earthquake. The waveforms recorded from ten earthquakes were analyzed using deconvolution interferometry. The waveforms at various depths were deconvolved by the waveforms recorded at the surface in order to identify predominant frequencies, shear-wave velocity profile, shear modulus and soil dynamic damping. To quantify the site amplification, surface-to-downhole traditional spectral ratio (SSR), response spectral ratio (RSR), cross-spectral ratio (cSSR), and horizontal-to-vertical spectral ratio (HVSR) were calculated. The site characteristic information obtained here can be used for soil-structure interaction analysis of a nearby twenty-story steel-moment frame building (Atwood Building), also instrumented.

The key findings of this study are as follows:

- The simplicity and similarity of the deconvolved waveforms from ten earthquakes manifest that a one-dimensional shear-beam model is accurate enough to represent the linear-elastic soil response at the DPK array under low intensity shaking.
- The deconvolution results in shear-wave velocities within 15% of the logged data. The maximum discrepancy in shear-wave velocities on average of borehole levels between different events is 17%. This suggests that the deconvolution interferometry is an effective way to quantify the shear-wave velocity profile for geotechnical arrays lacking in-situ measurements.
- The predominant soil frequency derived from the average shear-wave velocity is a crude estimation that is less accurate than the estimation from frequency-response function (FRF). For all earthquakes, the predominant frequency derived from the shear-wave velocity of the soil column is on average 1.2 Hz, which is 17% smaller than 1.44 Hz

estimated from the FRFs.

- Despite high aleatoric variability in earthquake waveforms, which come from events varying in size, distance and azimuth, the average shear-wave velocity of soil layers, and the predominant frequency of the soil column are consistent; this indicates that the soil properties remained linear-elastic during different earthquakes.
- Destructive interference phenomena were demonstrated to yield overestimation of site response by means of the surface-to-borehole transfer function with the exception of HVSR estimates in the low frequency range. The SSR method was found to be the least reliable one as compared to cSSR, HVSR and RSR techniques because it is very sensitive to the noise level, thus it is not a convenient method for computing site amplification using downhole recordings.
- The RSR method was found to be applicable only for computing site amplification at low frequencies (less than 4 Hz); its accuracy quickly diminishes at high frequencies.
- The HVSR method was generally found to represent the fundamental resonance peak but not to determine precisely amplification levels, a conclusion also drawn by others.
- The cSSR method can predict site amplification more reliably by removing the potential destructive interference, thus it is theoretically more accurate than the other methods. cSSR resulted in average site amplification as large as 3.5 at low frequencies (1.1-1.5 Hz) close to the first-mode frequency of the soil column. Other studies find on average that the largest site amplifications are on the lower-velocity NEHRP class D ($180 < V_{S30} < 360$ m/s) sites in Anchorage, with average amplifications around 3.0 at low frequencies (0.5–2.5 Hz). We found site amplification 17% higher than the average amplification reported by others.

DATA AND RESOURCES

Instruments of the National Strong Motion Network of USGS collected recordings used in this study. The records are available from the first author upon request. Figure 3 is modified from *http://nees.ucsb.edu/facilities/atwood-building-anchorage* (last accessed July, 2016).

ACKNOWLEDGMENTS

The authors thank Jack Boatwright, Mehran Rahmani, Brad Aagaard, Sebastiano D'Amico and an anonymous reviewer for their reviews and providing valuable suggestions and comments, which helped improving technical quality of this article. Special thanks are extended to Utpal Dutta and Joey Yang for discussions on DPK array soil properties, Luke Blair for generating the regional maps, Shahneam Reza for preparing the DPK array illustration, Jamie Steidl for making the ground motion recordings available, Christopher Stephens for processing the waveforms, and USGS's National Strong Motion Network technicians, James Smith, Jonah Merritt and Jason De Cristofaro for keeping the DPK array up and running. China Research Council provided the financial support for Weiping Wen and Fei Wang.

REFERENCES

Aki, K. (1957). "Space and time spectra of stationary stochastic waves, with special reference to microtremors", *Bull. Earthquake Res. Inst.*, Univ. of Tokyo, 35, 415–456.

Aki, K., and Richards, P.G. (2002). Quantitative seismology, University Science Books, Mill Valley, California.

Arai, H. and Tokimatsu, K. (2004). "S-Wave Velocity Profiling by Inversion of Microtremor H/V

Spectrum", *Bull. Seismol. Soc. Am.*, 94(1): 53-63, doi: 10.1785/0120030028.

Assimaki, D., Li, W., Steidl, J.H. and Tsuda, K. (2008). "Site amplification and attenuation via downhole array seismogram inversion: a comparative study of the 2003 Miyagi-Oki aftershock sequence", *Bull. Seismol. Soc. Am.*, 98(1): 301-330.

Bakulin, A. and Calvert, R. (2006). "The virtual source method: Theory and case study", *Geophysics*, 71(4): S139–S150.

Bonilla, L.F., Steidl, J.H., Lindley, G.T., Tumarkin, A.G. and Archuleta, R.J. (1997). "Site amplification in the San Fernando Valley, California: variability of site-effect estimation using the S-wave, coda, and H/V methods", *Bull. Seismol. Soc. Am.* 87, 710–730.

Boore, D.M. (2004). "Ground motion in Anchorage, Alaska, from the 2002 Denali fault earthquake: Site response and displacement pulses", *Bull. Seism. Soc. Am.,* 94: S72-S84.

Borcherdt, R.D. (1970). "Effects of Local Geology on Ground Motion Near San Francisco Bay", *Bull. Seism. Soc. Am., 60*: *29*–61.

Brocher, T.M., Filson, J.R., Fuis, G.S., Haeussler, P.J., Holzer, T.L., Plafker, G., and Blair, J.L. (2014). The 1964 Great Alaska Earthquake and tsunamis—A modern perspective and enduring legacies: U.S. Geological Survey Fact Sheet 2014–3018, 6 p., http://dx.doi.org/10.3133/fs20143018.

Bruhn, R.L. (1979). Holocene displacements measured by trenching the Castle Mountain Fault near Houston, Alaska: Alaska Division of Geological and Geophysical Surveys Geologic Report 61, p. 1-4.

Claerbout, J.F. (1968). "Synthesis of a layered medium from its acoustic transmission response", *Geophysics*, 33(2): 264–269.

Dutta, U., Biswas, N., Martirosyan, A., Papageorgiou, A. and Kinoshita, S. (2003). "Estimation of earthquake source parameters and site response in Anchorage, Alaska, from strong-motion network data using generalized inversion method", *Phys. Earth Planet. Interiors,* 137: 13–29.

Field, E.H. (1996). Spectral amplification in a sediment-filled valley exhibiting clear basin-edge induced waves, *Bull. Seismol. Soc. Am*., 86: 991–1005.

Field, E.H. and Jacob, K.H. (1995). A comparison and test of various site response estimation techniques, including three that are non-reference site dependent, *Bull. Seismol. Soc. Am*. 85: 1127–1143.

Finno, R.J. and Zapata-Medina, D.G. (2014). "Effects of Construction-Induced Stresses on Dynamic Soil Parameters of Bootlegger Cove Clays", *J. Geotech. Geoenviron. Eng.,* 140(4): 04013051, doi: 10.1061/(ASCE)GT.1943- 5606.0001072.

Fogelman, K., Stephens, C., Lahr, J.C., Helton, S. and Allen, M. (1978). Catalog of earthquakes in southern Alaska, October-December, 1977: U.S. Geological Survey Open-File Report 78-1097, 28 p.

Hartman, D.C., Pessel, G.H. and McGee, D.L. (1974). Stratigraphy of the Kenai group, Cook Inlet, Alaska Div. Geol. Geophys. Surv. Open-File Rept. 49. Available at http://www.dggs.alaska.gov/pubs/id/149 (last accessed November 2014).

Iwan, W.D. (1997). "Drift Spectrum: Measure of Demand for Earthquake Ground Motions", *ASCE Journal of Structural Engineering*, 123(4): 397-404.

Joyner, W.B., Warrick, R.E. and Oliver III, A.A. (1976). "Analysis of Seismograms from a Downhole Array In Sediments Near San Francisco Bay", *Bull. Seism. Soc. Am*., 66(3): 937-958.

Kitagawa Y, Okawa, I. and Kashima, T. (1992). "Observation and analyses of dense strong motions at sites with different geological conditions in Sendai", Proc. Int. Symp. on the Effects of Surface Geology on Seismic Motions, vol. 1. Assoc. of Earthquake Disaster Prevention; 25± 27:311±6.

Kudo, K., Sawada, Y. and Horike, M. (2004). "Current studies in Japan on H/V and phase velocity dispersion of microtremors for site characterization", *Proc. 13th World Conference on Earthquake Engineering*, Paper No. 1144.

Lachet, C. and Bard, P.Y. (1994). "Numerical and theoretical investigations on the possibilities and limitations of Nakamura's technique", *J. Phys. Earth,* 42: 377–397.

Lachet, C., Hatzfeld, D., Bard, P.Y., Theodulidis, N., Papaioannou, C. and Savvaidis, A. (1996). "Site effects and microzonation in the city of Thessaloniki (Greece) comparison of different approaches", *Bull. Seismol. Soc. Am.* 86(6): 1692–1703.

Lade, P.V., Updike, R.G. and Cole, D.A. (1988). Cyclic Triaxial Tests of the Bootlegger Cove Formation, Anchorage, Alaska: U.S. Geological Survey Bulletin 1825, 51 p.

Lahr, J.C., Page, R.A., Stephens, C.D. and Fogleman, K.A. (1986). "Sutton, Alaska, earthquake of 1984-evidence for activity on the Talkeetna segment of the Castle Mountain fault system", *Seismological Society of America Bulletin*, 76: 967-983.

Levenberg, K. (1944). A method for the solution of certain non-linear problems in least squares, *Quart. J. Appl. Maths*. II, no. 2, 164–168.

Li, J., Abers, G.A., Kim, Y. and Christensen, D. (2013). "Alaska megathrust 1: Seismicity 43 years after the great 1964 Alaska megathrust earthquake", *Journal of Geophysical Research: Solid Earth*, 118(9): 4861–4871.

Lobkis, O.I., and Weaver, R.L. (2001). "On the emergence of the Green's function in the correlations of a diffuse field", *J. Acoust. Soc. Am.*, 110: 3011–3017.

Marquardt, D. W. (1963). An Algorithm for Least-Squares Estimation of Nonlinear Parameters, *SIAM Journal on Applied Mathematics* 11, no. 2, 431–441.

Martirosyan, A., Dutta, U., Biswas, N., Papageorgiou, A., and Combellick, R. (2002). "Determination of site response in Anchorage, Alaska, on the basis of spectral ratio methods", *Earthquake Spectra*, 18(1): 85-104.

Nakata, N. and Snieder, R. (2012). "Estimating near-surface shear wave velocities in Japan by applying seismic interferometry to KiK-net data", *Journal of Geophysical Research*, 117: B01308.

Nakamura, Y. (1989). A method for dynamic characteristics estimation of subsurface using microtremor on the ground surface. QR Railway Technical Research Institute 30(1).

Nakata, N., Snieder, R., Kuroda, S., Ito, S., Aizawa, T. and Kunimi, T. (2013). "Monitoring a building using deconvolution interferometry, I: Earthquake-data analysis", *Bull. Seismol. Soc. Am.* 103(3): 1662– 1678, doi: 10.1785/0120120291.

Nath, S. K., Chatterjee, D., Biswas, N. N., Dravinski, M., Cole, D.A., Papageorgiou, A., Rodriguez, J.A., and Poran, C.J. (1997). "Correlation study of shear wave velocity in near surface geological formations in Anchorage, Alaska", *Earthquake Spectra* 13(1): 55-75.

Nath, S.K., Biswas, N.N., Dravinski, M.A. and Papageorgiou, A.S. (2002). "Determination of S-wave site response in Anchorage, Alaska in the 1–9 Hz frequency band", *Pure and applied geophysics*, 159(11-12): 2673-2698.

Newton, C. and Snieder, R. (2012). "Estimating intrinsic attenuation of a building using deconvolution interferometry and time reversal", *Bull. Seismol. Soc. Am.* 102(5): 2200-2208.

Parolai, S. and Richwalski, S. (2004). "The importance of converted waves in comparing H/V and RSM site response estimates", *Bull. Seismol. Soc. Am.* 94(1): 304–313.

Plafker, G., Gilpin, L.M. and Lahr, J.C. (1994). Neotectonic map of Alaska, in The Geology of North America, vol. G-1, The geology of Alaska (G. Plafker and H.C. Berg, eds.), Geol. Soc. Amer., Boulder, Colo., pp. 389-449.

Prieto, G.A., Lawrence, J.F., Chung, A.I. and Kohler, M.D. (2010). "Impulse response of civil structures from ambient noise analysis", *Bull. Seismol. Soc. Am.,* 100(5A): 2322-2328.

Rahmani M. and Todorovska M.I. (2013). "1D system identification of buildings from earthquake response by seismic interferometry with waveform inversion of impulse responses – method and application to Millikan Library", *Soil Dynamics and Earthquake* Engrg. 47:157-174, doi: 10.1016/j.soildyn.2012.09.014.

Riepl, J., Bard, P.Y., Hatzfeld, D., Papaioannou, C. and Nechtschein, S. (1998). "Detailed evaluation of site-response estimation methods across and along the sedimentary valley of Volvi (EURO-SEISTEST)", *Bull. Seismol. Soc. Am.,* 88(2): 488–502.

Roux, P. and M. Fink (2003). "Green's function estimation using secondary sources in a shallow wave environment", *J. Acoust. Soc. Am.*, 113: 1406–1416.

Safak, E. (1997). "Models and methods to characterize site amplification from a pair of records", *Earthquake Spectra*, 13(1): 97-129.

Safak, E. (2001). "Local site effects and dynamic soil behavior", *Soil Dyn. and Eq. Eng.*, 21: 453-458.

Schuster, G.T., Yu, J., Sheng, J. and Rickett, J. (2004). "Interferometric daylight seismic imaging", *Geophys. J. Int.*, 157: 838–852.

Shearer, P. M., and J. A. Orcutt (1987). "Surface and near-surface effects on seismic waves: theory and borehole seismometer results", *Bull. Seismol. Soc. Am*., 77: 1168–1196.

Smart, K.J., Pavlis, T.L., Sisson, V.B., Roeske, S.M. and Snee, L.W. (1996). "The Border Ranges fault system in Glacier Bay National Park, Alaska: Evidence for major early Cenozoic dextral strike-slip motion", *Canadian Journal of Earth Sciences* 33(9): 1268-1282.

Snieder, R. and Safak, E. (2006). "Extracting the Building Response Using Seismic Interferometry: Theory and Application to the Millikan Library in Pasadena, California", *Bull. Seism. Soc. Am.,* 96(2): 586–598.

Snieder, R., Sheiman, J. and Calvert, R. (2006). "Equivalence of the virtual-source method and wave-field deconvolution in seismic interferometry", *Physical Review*, E 73, 066620.

Steidl, J.H. (2006). "Inventory of Existing Strong-Motion Geotechnical Arrays", Proceedings of the International Workshop for International Workshop for Site Selection, Installation, and Operation of Geotechnical Strong-Motion Arrays Workshop 2: Guidelines for Installation, Operation, and Data Archiving and Dissemination, La Jolla, California, Cosmos Publication No. CP-2006/01 (*http://www.cosmos-eq.org/publications/CP-2006-01.pdf*).

Steidl, J.H., Tumarkin, A.G. and Archuleta, R.J. (1996). "What is a reference site?", *Bull. Seismol. Soc. Am.,* 86: 1733–1748.

Trampert, J., Cara, M. and Frogneux, M. (1993). "SH propagator matrix and QS estimates from borehole- and surface-recorded earthquake data", *Geophysical Journal International* 112:290–299.

Ulery, C.A., Updike, R.G. and USGS Office of Earthquakes (1983). "Subsurface structure of the cohesive facies of the Bootlegger Cove formation, southwest Anchorage: Alaska", Division of Geological & Geophysical Surveys Professional Report 84, 5 p., 3 sheets, scale 1:15,840.

Updike, R.G. and Carpenter, B.A. (1986). "Engineering Geology of the Government Hill Area, Anchorage, Alaska", *U.S. Geol. Surv. Bull.*,1588, 36 pp.

Updike, R.G. and Ulery, C.A. (1986). Engineering - geologic map of southwest Anchorage, Alaska: Alaska Division of Geological & Geophysical Surveys Professional Report 89, 1 sheet, scale 1:15, 840. doi:10.14509/2270.

Yang, Z., Dutta, U., Xiong, F., Biswas, N. and Benz, H. (2008). "Seasonal frost effects on the dynamic behavior of a twenty-story office building", *Cold Regions Sc. & Techn.* 51:76-84.

Wen, W. and Kalkan, E. (2016). "Interferometric System Identification—An Application to a Twenty-story Instrumented Building in Anchorage, Alaska", *Bull. Seismol. Soc. Am*. (in-review).

Wong I., Dawson, T., Dober, M. and Hashash, Y. (2010). "Evaluating the seismic hazard in Anchorage, Alaska", *Proc. of the 9th U.S. National and 10th Canadian Conference on Earthquake Engineering,* July 25-29, Toronto, Ontario, Canada, paper no: 785.

Zerva, A (2009). Spatial variation of seismic ground motions: modeling and engineering applications. CRC Press. ISBN ISBN-10: 0849399297; ISBN-13: 978-0849399299.

TABLES

Table 1. List of Abbreviations and Symbols Present in This Article

BCF	Bootlegger Cove formation
c	Wave speed
C_{xy}	Coherence
cSSR	Surface-to-borehole cross-spectral ratio
DPK	Delaney Park
FAS	Fourier amplitude spectrum
FRF	Frequency response function
G_n	Shear modulus of n^{th} layer
H	Total height of soil column
HVSR	Horizontal-to-vertical spectral ratio
L	Wave travel distance
M	Moment magnitude
RSR	Surface-to-borehole response spectral ratio
Q	Quality factor
r	Reflection coefficient
P_{xx}	Power spectral density of waveform x
P_{xy}	Cross power spectral density of waveforms x and y
PGA	Peak ground acceleration
$s(t)$	Excitation source at fixed-base
SSR	Surface-to-borehole standard spectral ratio
t	Time instant
u	Soil response
V_S	Shear-wave velocity
V_{S30}	Average shear-wave velocity of upper 30 m of crust
w	Cyclic frequency
z	Height
ρ_n	Wet density of n^{th} layer
ξ	Damping ratio

τ	Wave travel time

Table 2. Origin Times, Magnitudes, Epicenters of Local and Regional Earthquakes Recorded by The Delaney Park Borehole Array in Anchorage Alaska between 2006 and 2013 (See "Data and Resources")

Event No.	Origin time (UTC) (y-m-d)	Moment Magnitude	Epicenter Coordinates Latitude(°)	Longitude(°)	Depth (km)	Epicentral Distance (km)	Peak Acceleration (cm/s^2)
1	2013-03-13	5.4	62.559	-151.071	83.6	162.0	1.07
2	2012-05-16	4.6	61.118	-149.926	61.7	10.8	17.66
3	2011-06-16	5.1	60.765	-151.076	58.9	81.1	7.78
4	2010-09-20	4.9	61.115	-150.219	45.4	20.7	30.53
5	2010-07-08	4.8	61.805	-150.505	14.9	73.5	6.57
6	2010-04-07	4.6	61.580	-149.652	35.3	42.7	3.62
7	2009-08-19	5.1	61.228	-150.858	66.4	51.7	5.44
8	2009-06-22	5.4	61.939	-150.704	64.6	91.5	11.64
9	2006-09-06	4.5	61.621	-149.930	40.7	45.4	2.94
10	2006-07-27	4.7	61.155	-149.678	36.0	13.3	13.86

The earthquakes are numbered sequentially according to their origin times. Peak acceleration is the observed absolute maximum amplitude of the waveforms from the accelerometers at the surface level

Table 3. Average Shear-wave Velocity of Soil Layers and Soil Column Identified based on Upward and Downward Traveling Waves; Unit = m/s

Event No.	Layer 1 (0 - 10.7 m)		Layer 2 (10.7 - 18.3 m)		Layer 3 (18.3 - 30.5 m)		Layer 4 (30.5 - 45.4 m)		Layer 5 (45.4 - 61 m)		Average shear-wave velocity of soil
	(up)	(down)	(up)	(down)	(up)	(down)	(up)	(down)	(up)	(down)	
1	305.7	305.7	253.3	253.3	244.0	244.0	270.9	298.0	780.0	624.0	295
2	267.5	267.5	304.0	253.3	221.8	271.1	298.0	298.0	780.0	624.0	293
3	267.5	267.5	253.3	304.0	271.1	244.0	270.9	298.0	780.0	624.0	293
4	305.7	305.7	217.1	253.3	271.1	244.0	270.9	298.0	780.0	624.0	294
5	267.5	305.7	304.0	253.3	244.0	244.0	270.9	298.0	780.0	624.0	294
6	305.7	267.5	253.3	304.0	244.0	244.0	270.9	298.0	780.0	624.0	292
7	305.7	305.7	253.3	253.3	244.0	271.1	298.0	270.9	624.0	624.0	297
8	267.5	305.7	253.3	253.3	271.1	244.0	270.9	298.0	780.0	624.0	294
9	305.7	267.5	253.3	304.0	244.0	244.0	270.9	298.0	780.0	624.0	296
10	267.5	267.5	253.3	253.3	271.1	244.0	331.1	298.0	624.0	624.0	295
Average	286.6	286.6	259.8	268.5	252.6	249.4	282.3	295.3	748.8	624.0	
Std. dev.	20.1	20.1	25.9	24.5	17.3	11.4	20.5	8.6	65.8	0	

Table 4. Site Fundamental Frequencies Derived from Shear-wave Velocity and Spectral Ratios; Unit = Hz

Event No.	Derived frequency, *f*	First-mode frequency	Second-mode frequency	Third-mode frequency
1	1.209	1.563	4.126	6.934
2	1.201	1.392	3.931	6.909
3	1.201	1.440	4.028	6.958
4	1.205	1.392	4.004	6.812
5	1.205	1.489	4.004	6.934
6	1.197	1.416	4.077	6.982
7	1.217	1.416	4.077	6.958
8	1.205	1.465	4.053	6.982
9	1.213	1.465	4.150	7.031
10	1.209	1.416	4.126	6.836
Average	1.206	1.445	4.060	6.934
Std. dev.	0.006	0.053	0.068	0.067

Table 5. Mean Slope of Natural Logarithm Envelope at Different Boreholes Shown in Figure 12, Quality Factor Q, and Damping Ratio ξ Computed from Ten Earthquakes

Event No.	Mean slope of different layers	Quality factor (Q)	Damping ratio (ξ)
1	-0.415	11.824	0.042
2	-0.399	10.960	0.046
3	-0.426	10.627	0.047
4	-0.405	10.800	0.046
5	-0.412	11.365	0.044
6	-0.394	11.296	0.044
7	-0.397	11.197	0.045
8	-0.401	11.469	0.044
9	-0.404	11.392	0.044
10	-0.419	10.617	0.047
Average	-0.407	11.155	0.045
Std. dev.	-0.104	0.395	0.002

FIGURES

Figure 1. Photo showing Delaney Park (DPK) borehole array in downtown Anchorage Alaska. Atwood building (twenty-story steel moment frame) in the background (165 m away from DPK array) is also instrumented. Google map insert shows the location of Delaney Park (photo = E. Kalkan). The color version of this figure is available only in the electronic edition.

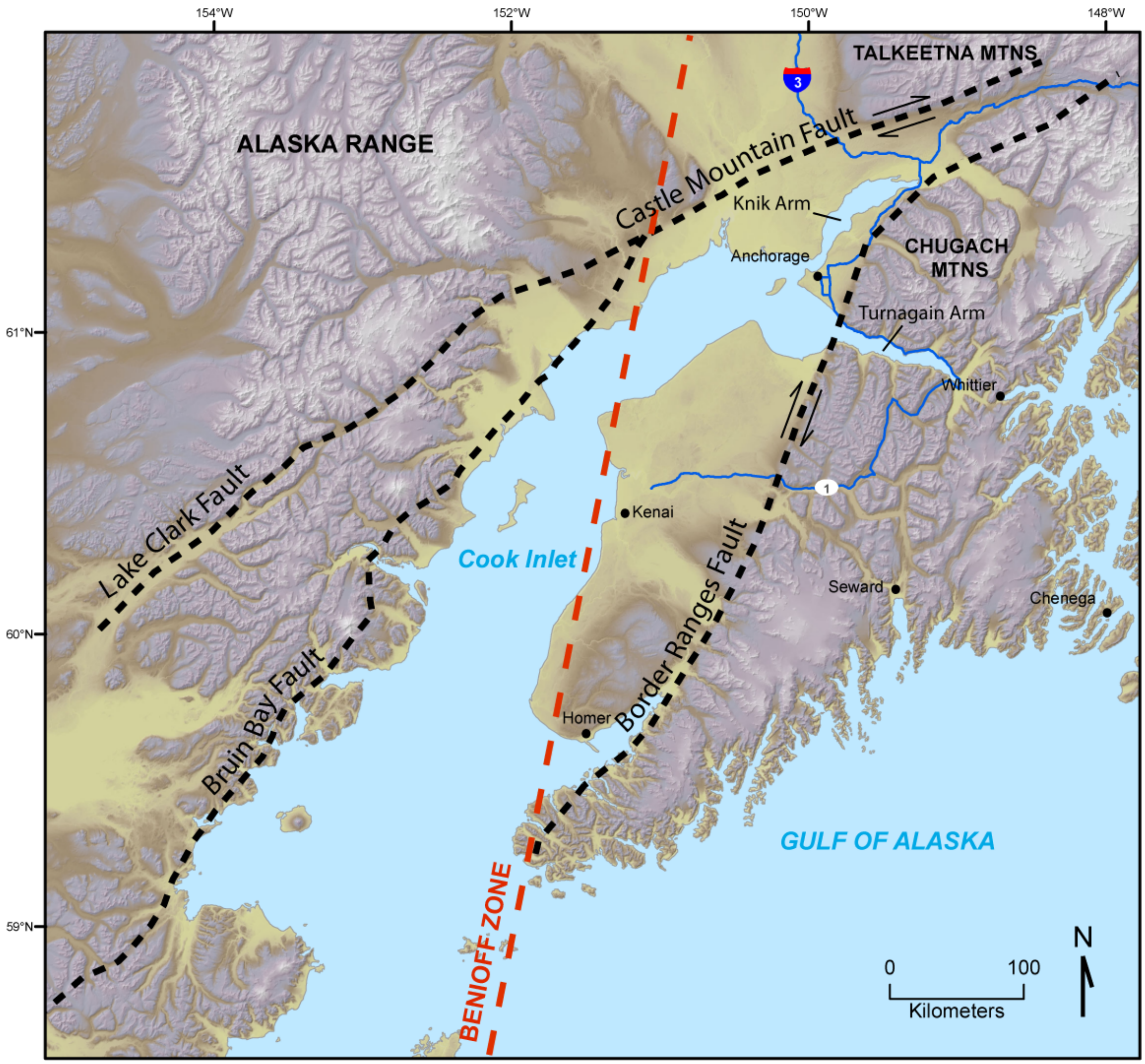

Figure 2. Active faults in the vicinity of Anchorage Alaska, shown by dash lines; major highways are denoted, dots indicate cities. Map is modified from Lade et al. (1988), Benioff zone contour is from Plafker et al. (1994). The color version of this figure is available only in the electronic edition.

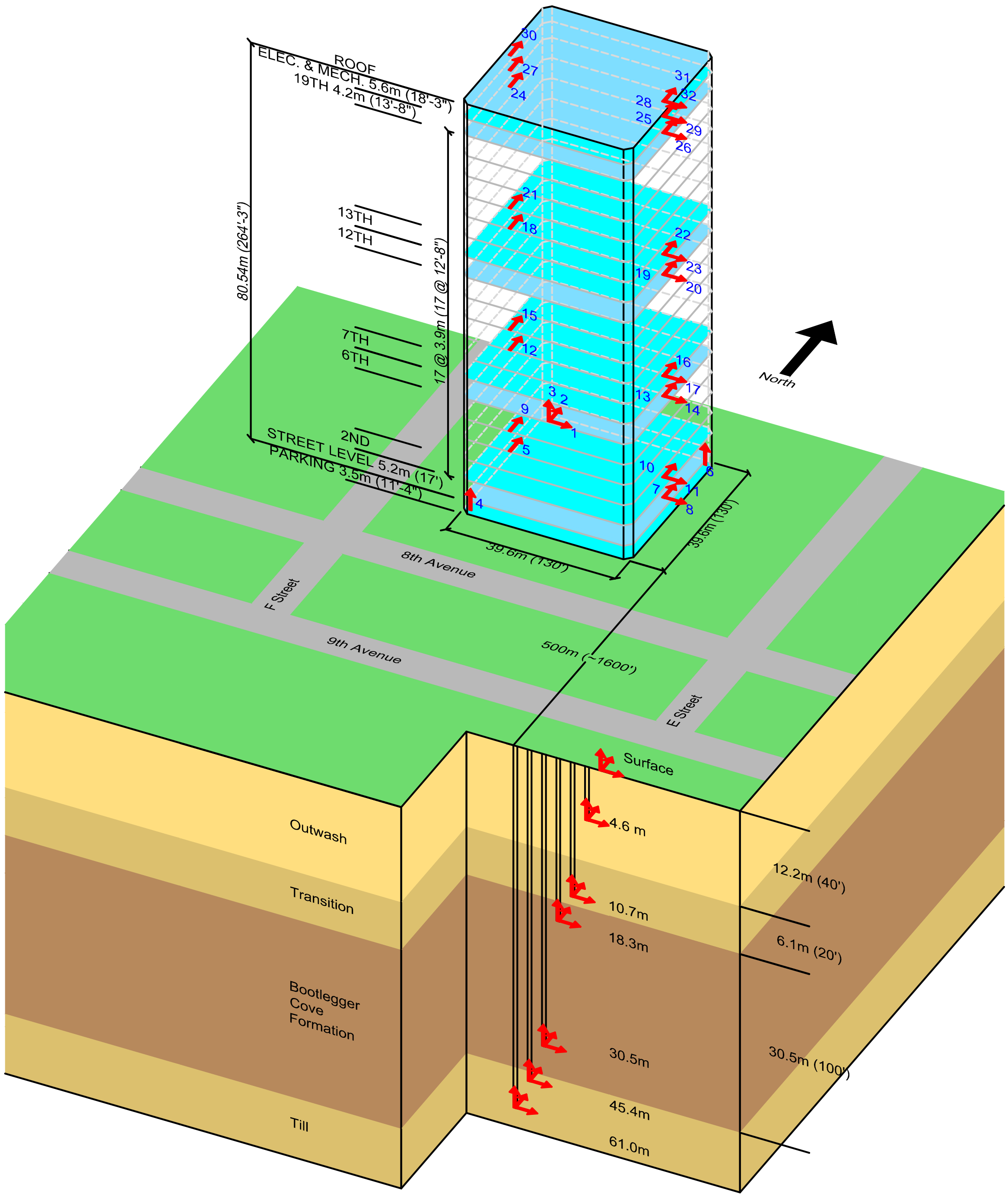

Figure 3. Instrumentation layout of Delaney Park borehole array and soil layers; arrows indicate sensor orientation. Also shown is the instrumentation layout of Atwood building (see "Data and Resources"). The color version of this figure is available only in the electronic edition.

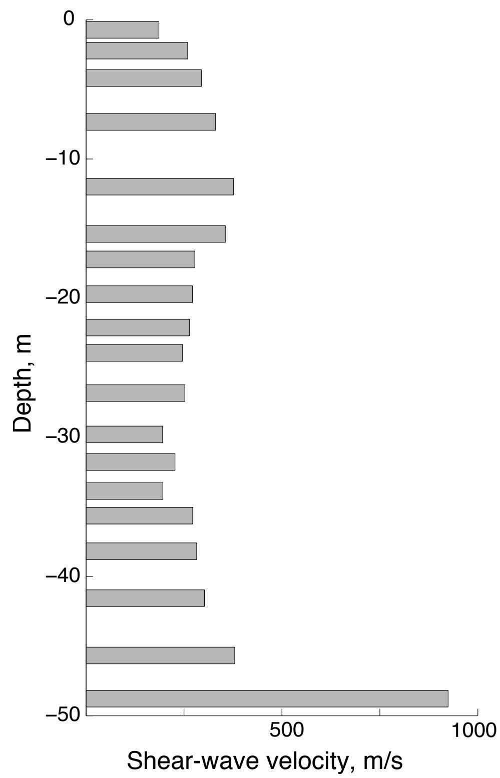

Figure 4. Shear-wave velocity with depth based on geophysical measurements at a site about 200 m away from the DPK [adapted from Nath et al. (1997) and Yang et al. (2008)]. Shear-wave velocity is lower between -20 and -48 m at Bootlegger Cove formation than the shallower glacial outwash (between 0 and -12.2 m) (see also Figure 3 for geological profile).

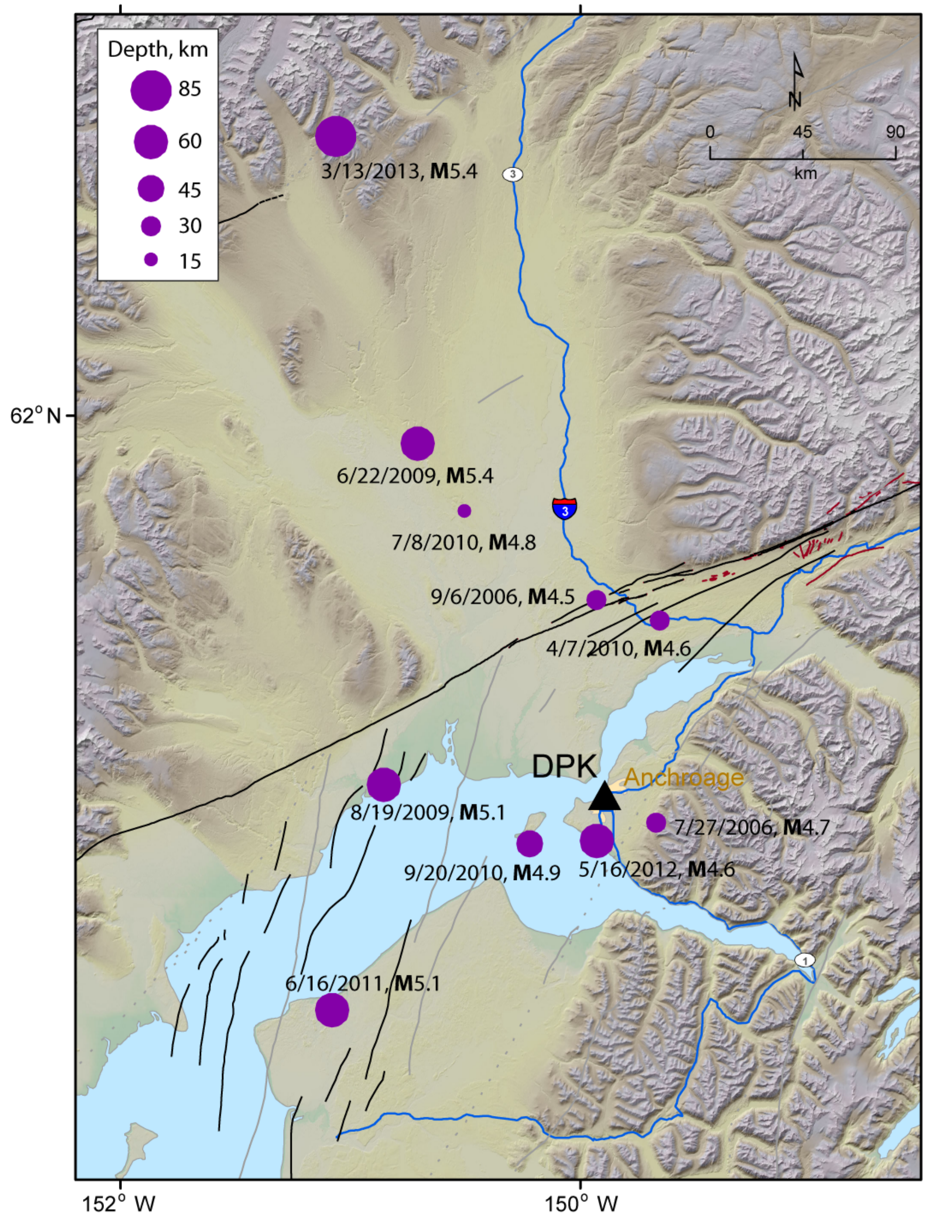

Figure 5. Map showing location of Delaney Park borehole array by triangle (N61.21349° and W149.98328°) and epicenters of selected ten earthquakes with circles (summarized in Table 1). Quaternary faults and major highways are indicated in and around Anchorage, Alaska. The color version of this figure is available only in the electronic edition.

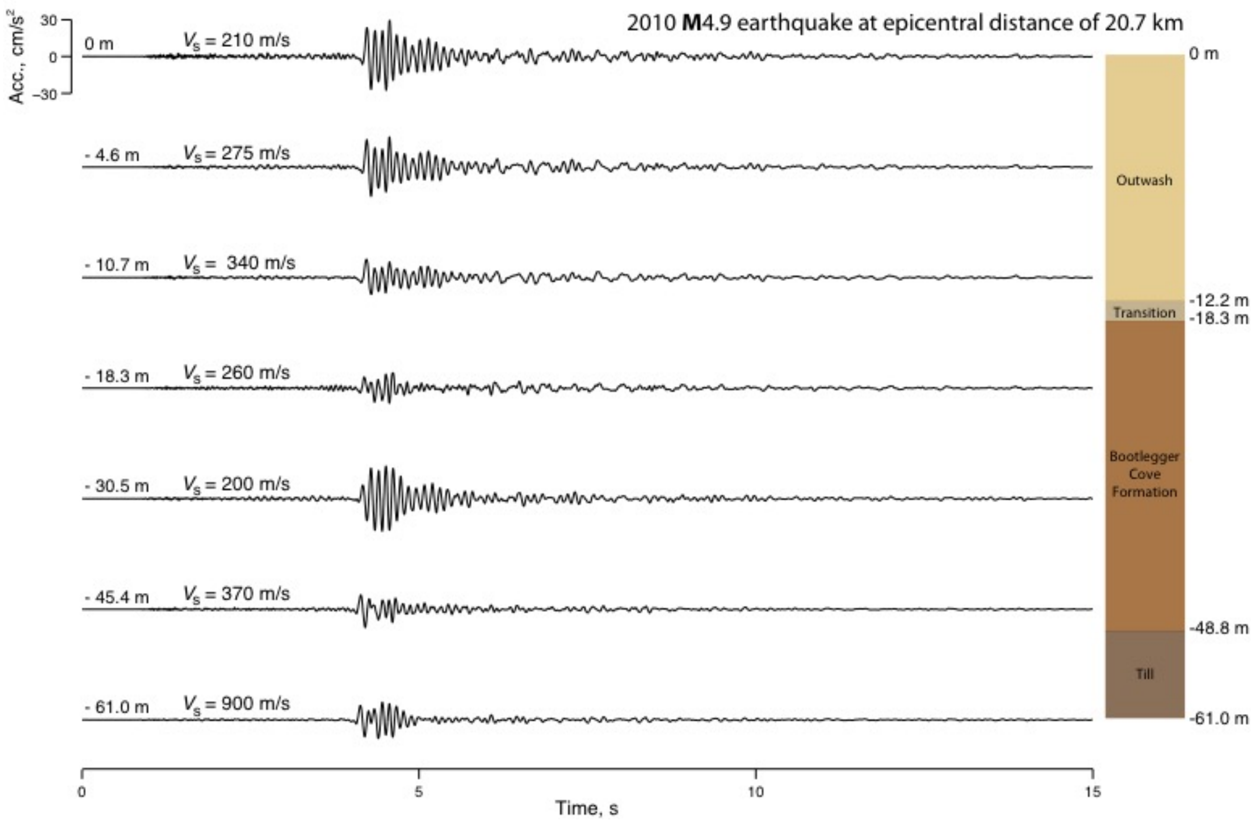

Figure 6. Horizontal acceleration waveforms from the 2010 **M**4.9 earthquake at epicentral distance of 20.7 km; recorded peak ground acceleration at the surface is 30.53 cm/s^2; soil layers and their V_S values are depicted. Only first 15 s of the waveforms are shown; minimum duration of records is 222 s. The color version of this figure is available only in the electronic edition.

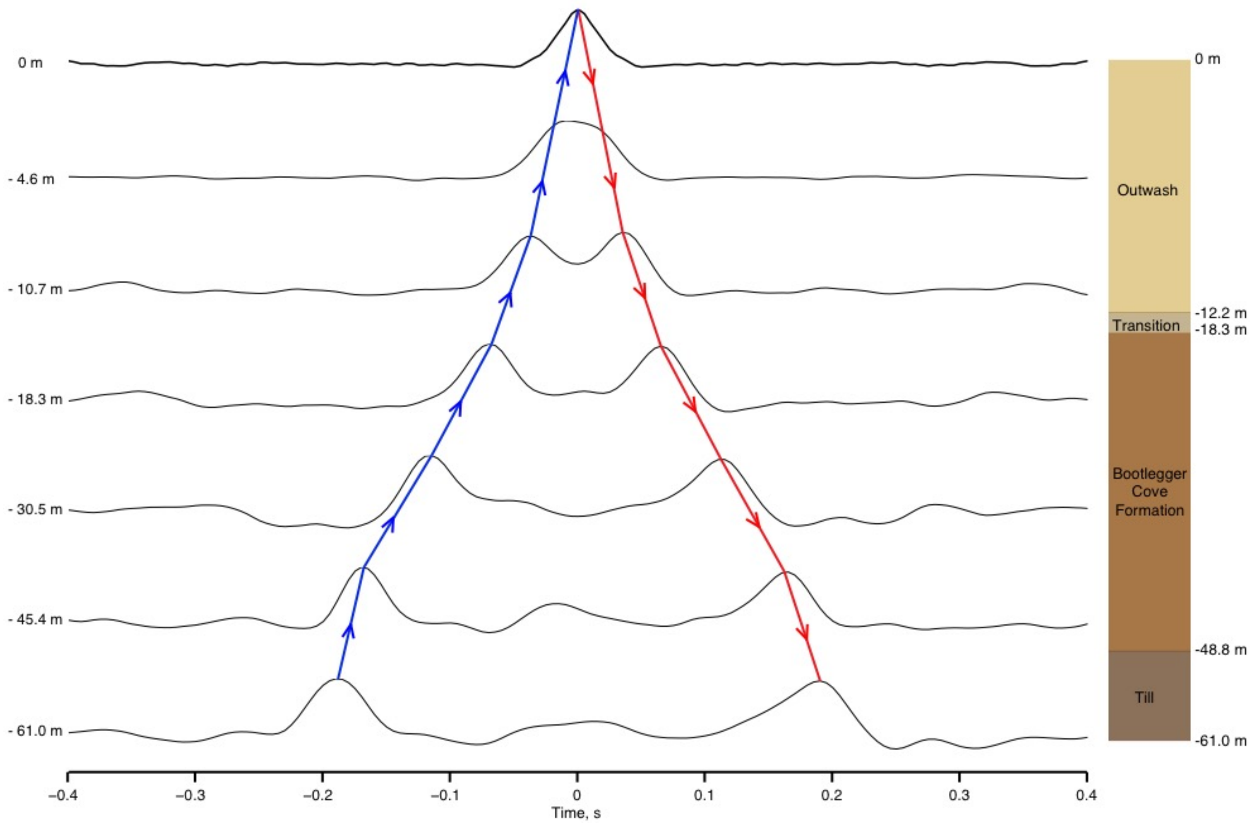

Figure 7. Waveforms in Figure 6 at different depths after deconvolution with the waveform recorded at the surface. The deconvolved waveforms by the surface response are acausal, and show the upward and downward traveling waves. At the second depth (close to the surface) these waves are not distinguishable due to overlapping. The color version of this figure is available only in the electronic edition.

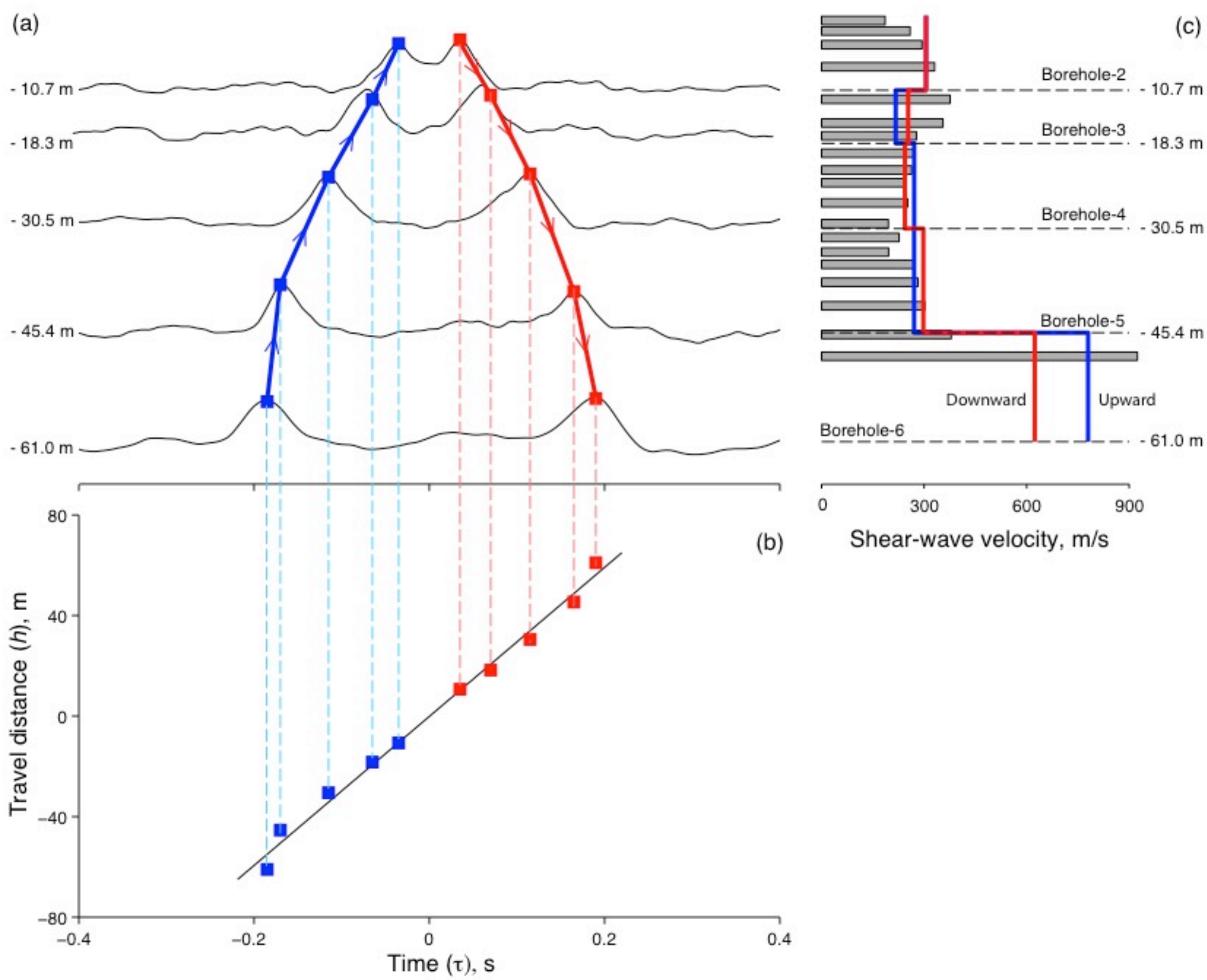

Figure 8. Plots show (a) arrival times of upward and downward traveling waves at five borehole levels estimated from the peaks of the deconvolved waves; (b) an average shear-wave velocity for the upper 61 m soil deposit is derived from the estimated travel times (τ) and the distances (h) following a least square fit; (c) comparisons of estimated shear-wave velocity profile with logged data; dashed horizontal lines indicate depths of borehole sensors. Upward and downward traveling waves are identified by arrows. Results are based on the 2010 **M**4.9 earthquake waveforms shown in Figure 6. The color version of this figure is available only in the electronic edition.

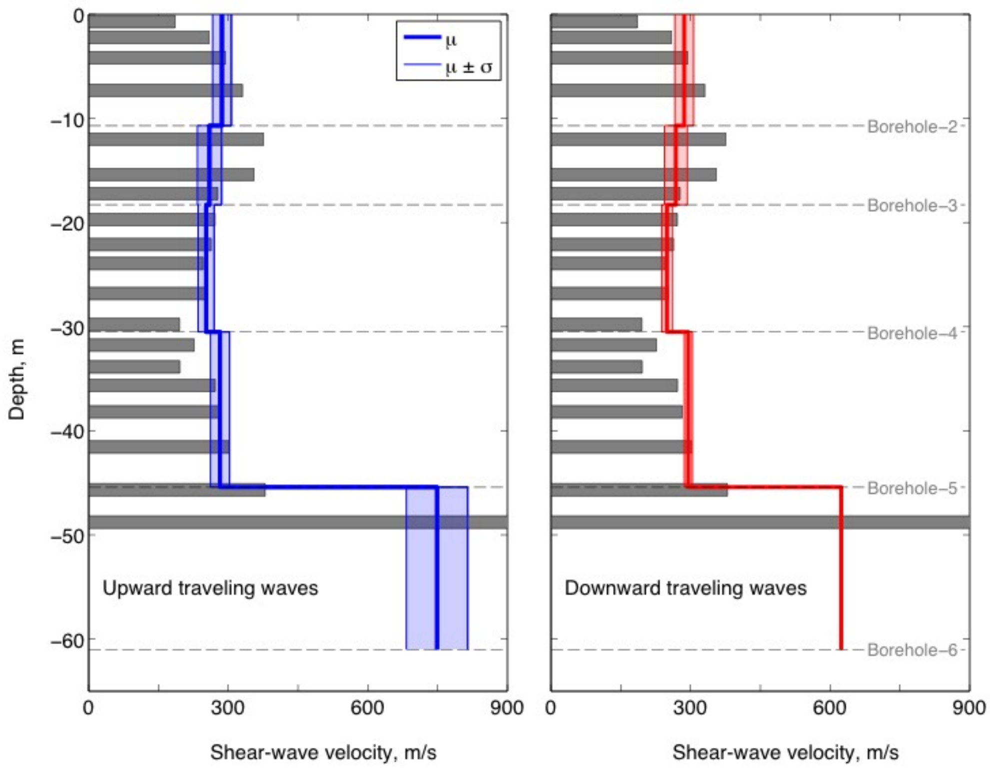

Figure 9. Plots show comparisons of estimated mean (thick vertical lines) and mean ± one standard deviation (thin vertical lines) shear-wave velocity profiles using ten earthquakes with logged data. The dashed horizontal lines indicate depths of borehole sensors. The color version of this figure is available only in the electronic edition.

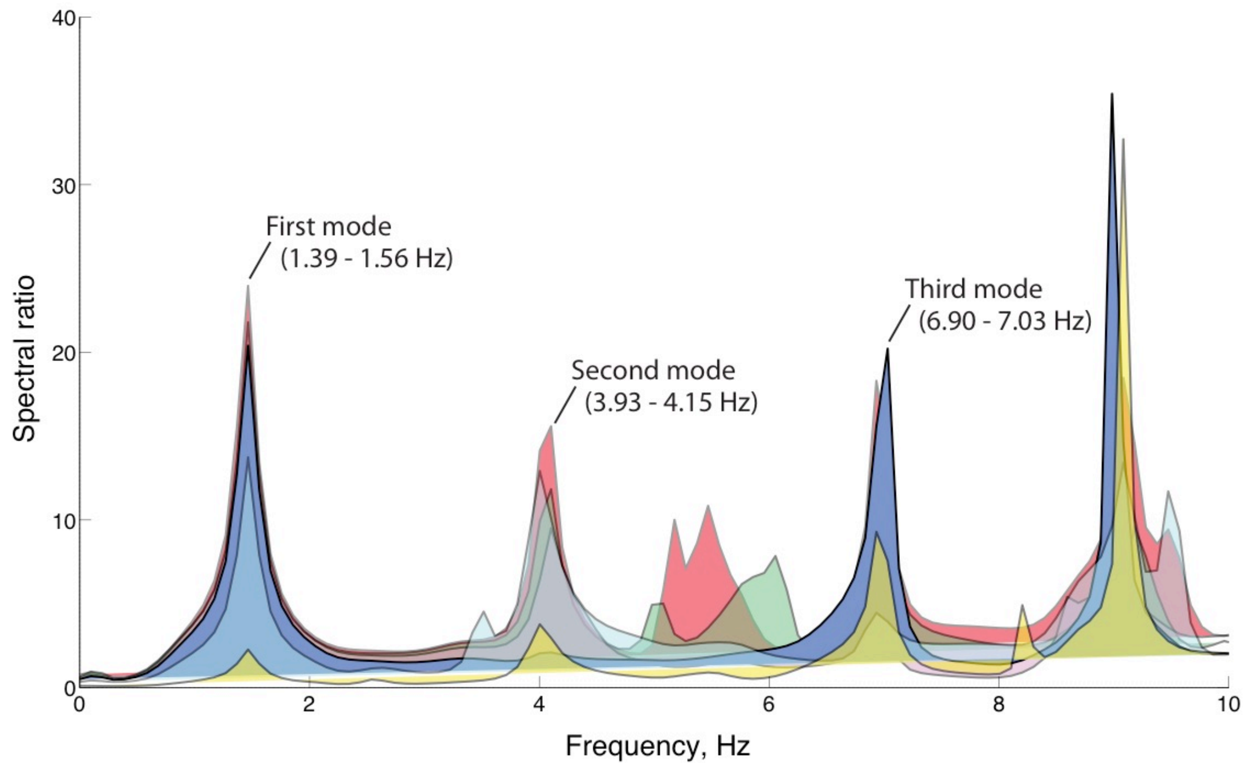

Figure 10. First three fundamental frequencies of the soil column identified on horizontal spectral ratios between the surface and -61 m (deepest borehole). Plots are based on waveforms from ten earthquakes. Note that peak at 9 Hz denotes the fourth mode. - The color version of this figure is available only in the electronic edition.

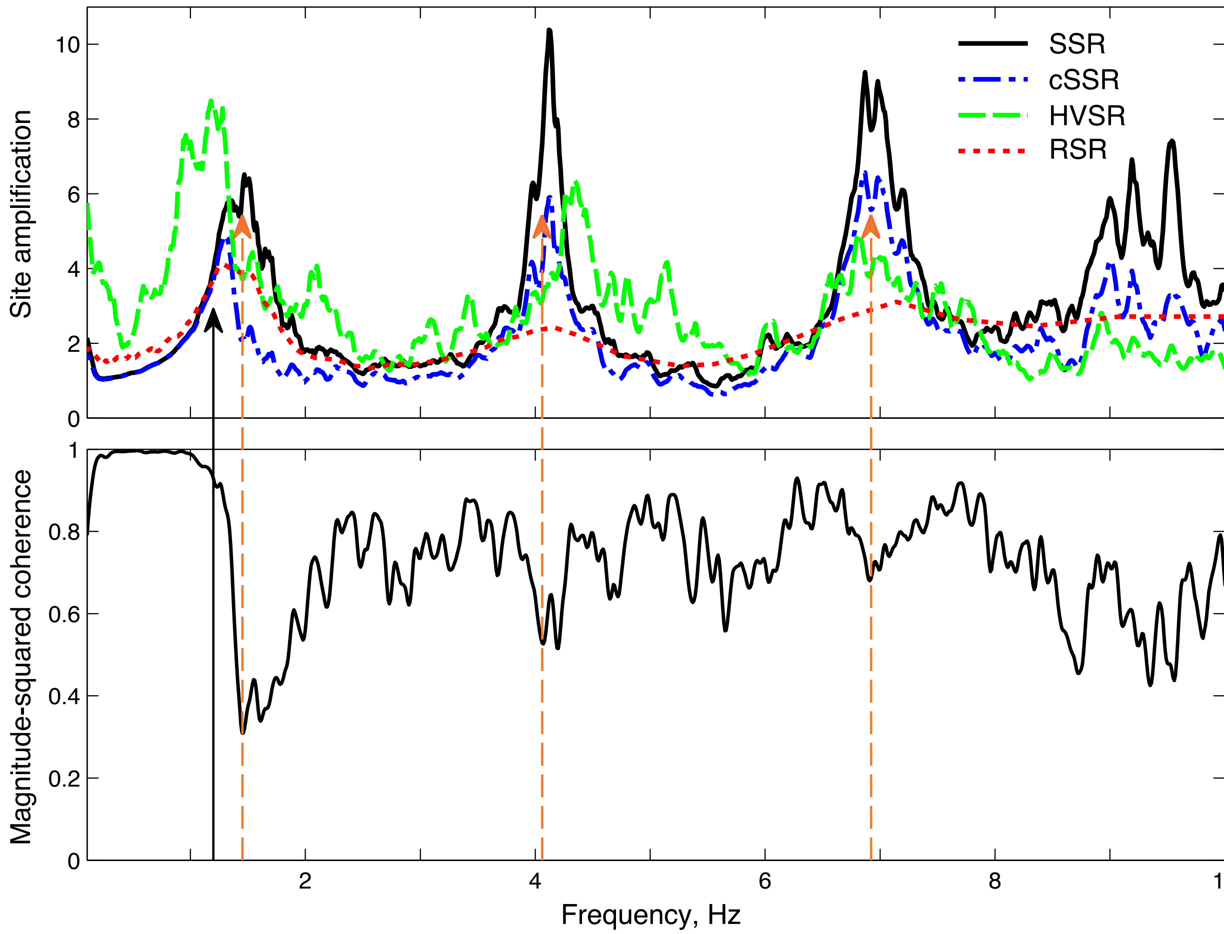

Figure 11. Average site amplification estimates of recordings from ten earthquakes calculated with four different methods [surface-to-downhole traditional spectral ratio (SSR), response spectral ratio (RSR), cross-spectral ratio (cSSR), and horizontal-to-vertical spectral ratio (HVSR)]. Also shown are the corresponding average magnitude-squared coherence estimates of the surface and the deepest borehole recordings. The solid vertical line with arrow indicates the first-mode frequency with high coherence, the dashed vertical lines with arrows denote the frequencies where the sinks of coherence estimate are observed due to destructive interference. The color version of this figure is available only in the electronic edition.

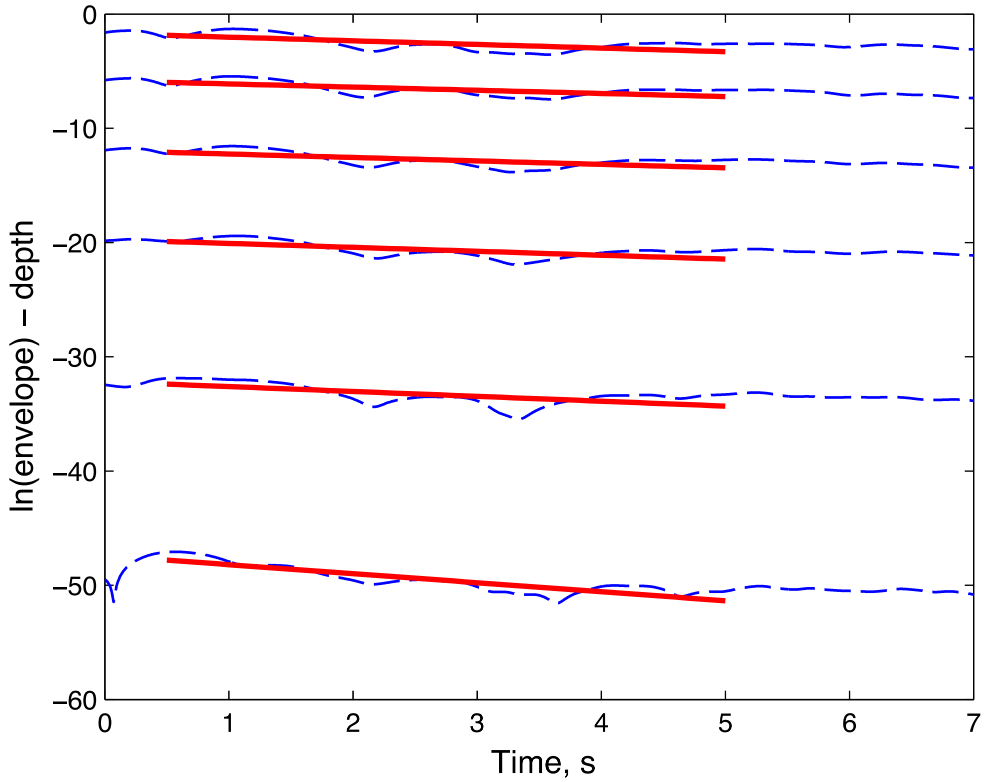

Figure 12. Natural logarithm envelope of the bandpass-filtered waveforms (dashed lines), and their least-square fit between 0.5 s and 5 s (solid lines). Data correspond to the **M**4.9 earthquake as shown in Figure 6. Deconvolved waves were bandpass filtered by a 4th order acausal Butterworth filter with cutoff frequencies of 0.5 and 2 Hz. The color version of this figure is available only in the electronic edition.